



Application of computed tomography-based radiomics combined with clinical factors in the diagnosis of malignant degree of lung adenocarcinoma

Liang Shi[#], Maoyuan Yang[#], Jie Yao, Haoxiang Ni, Hancheng Shao, Wei Feng, Ziyi He, Bin Ni

Department of Thoracic Surgery, The First Affiliated Hospital of Soochow University, Suzhou, China

Contributions: (I) Conception and design: B Ni, L Shi; (II) Administrative support: B Ni; (III) Provision of study materials or patients: M Yang, J Yao, H Ni, H Shao; (IV) Collection and assembly of data: L Shi, M Yang, W Feng, Z He; (V) Data analysis and interpretation: L Shi, M Yang; (VI) Manuscript writing: All authors; (VII) Final approval of manuscript: All authors.

[#]These authors contributed equally to this work.

Correspondence to: Bin Ni, PhD, Department of Thoracic Surgery, The First Affiliated Hospital of Soochow University, 188 Shizi Street, Gusu District, Suzhou 215006, China. Email: nb_fyywk@163.com.

Background: As an emerging technology, radiomics is being widely used in the diagnosis of early lung cancer due to its excellent diagnostic performance. However, there is a lack of studies that apply radiomics to the diagnosis of malignancy of lung adenocarcinoma. Thus, we used computed tomography (CT)-based radiomics to construct a model for the diagnosis of high-risk lung adenocarcinoma.

Methods: Data of 170 patients who underwent surgical treatment at the First Affiliated Hospital of Soochow University and had a maximum nodule diameter ≤ 2 cm on preoperative CT images between January 2020 and December 2021 were retrospectively analyzed. All enrolled patients were randomly divided into experimental and validation groups according to the ratio of 7:3. The diagnosis of lung adenocarcinoma was based on postoperative pathological results. The region of interest was delineated on preoperative CT images, and the radiomics features were extracted. The least absolute shrinkage and selection operator (LASSO) was used to screen the radiomics features thus obtaining the radiomics score (Radscore), which was the basis of the radiomics model. Based on the multivariate regression analysis, independent predictors were screened from the clinical baseline data and imaging features thus constructing clinical model. Multivariate logistic regression was used to combine independent predictors and the Radscore to form a comprehensive nomogram. The diagnostic performance of constructed models was evaluated based on receiver operating characteristic (ROC) curves and decision curve analysis (DCA).

Results: The sensitivity and specificity of the clinical model based on consolidation-to-tumor ratio (CTR), lobulated signs and vascular anomaly signs was 70.0% and 76.7% in the validation group. The radiomics model [area under the curve (AUC) 0.926; 95% confidence interval (CI): 0.857–0.995] and the comprehensive model (AUC 0.922; 95% CI: 0.851–0.992) performed better than clinical model (AUC 0.839; 95% CI: 0.720–0.958) in the validation group. The sensitivity and specificity of the comprehensive model was 85.0% and 80.0% in the validation group. DCA of radiomics model and comprehensive model suggested they have better net survival benefit than clinical model.

Conclusions: Compared with clinical model, radiomics model and comprehensive model had better diagnostic performance in distinguishing malignant degree of lung adenocarcinoma.

Keywords: Early diagnosis; lung adenocarcinoma; pulmonary nodules; radiomics

Submitted Sep 20, 2022. Accepted for publication Nov 18, 2022.

doi: 10.21037/jtd-22-1520

View this article at: <https://dx.doi.org/10.21037/jtd-22-1520>

Introduction

Pulmonary lobectomy has long been considered the standard surgical treatment for early-stage lung cancer (1). Compared with lobectomy, sublobectomy (including segmentectomy and wedge resection) has a higher local recurrence rate and higher risk of death (2). With advancements in computed tomography (CT) imaging technology, an increasing number of small pulmonary nodules have been found in young people (3) and sublobectomy is gradually being used more often for the surgical treatment of early-stage lung cancer (4). The JCOG0804/WJOG4507L study indicated that for early-stage lung cancer with a tumor diameter ≤ 2 cm and a consolidation-to-tumor ratio (CTR) < 0.25 , sublobectomy can reduce surgery-related complications while ensuring safety, making it better than traditional lobectomy (5). Subsequently, the results of the JCOG0802/WJOG4607L study led by Japanese researchers showed that for stage IA lung cancer (tumor diameter ≤ 2 cm, CTR > 0.5), despite the presence of a higher risk of local recurrence, the 5-year survival rate of the segmentectomy group was higher than that of the lobectomy group. Therefore, segmentectomy can replace lobectomy as the standard surgical treatment for early-stage lung cancer (6) and so the selection of surgical method for early-stage lung cancer, especially for small pulmonary nodules with a diameter ≤ 2 cm on imaging, has been receiving more attention from surgeons.

On the other hand, even stage IA lung cancer has a high degree of malignancy and poor prognosis. In early-stage lung cancer with mainly invasive adenocarcinoma components, the presence of solid and micropapillary components, even if they comprise $\leq 5\%$, also indicates a worse prognosis (7,8). Patients with stage IA lung adenocarcinoma with spread through air spaces (STAS) are more likely to relapse after surgery (9), and for those patients, the prognosis of lobectomy is significantly better than that of sublobectomy (10). Pulmonary invasive mucinous adenocarcinoma is more prone to STAS, and thus more likely to recur and have a poor prognosis (11). Pathological results suggest that early-stage lung cancer patients with lymphovascular invasion (LVI) and visceral pleural invasion (VPI) have significantly reduced 5-year recurrence-free survival and overall survival (12-14). Previous studies (7,10-12) have shown that for patients whose postoperative pathological results suggest a high degree of tumor malignancy and a poor prognosis, lobectomy is more appropriate than sublobectomy if the patient's basic condition permits. Therefore, it is particularly important to select the best surgical approach based on accurate judgment of the preoperative malignancy of pulmonary nodules for good prognosis of patients.

With the rapid development of imaging equipment and image acquisition technology, radiomics has shown advantages over traditional image interpretation. Radiomics was first developed by the Dutch in 2012 (15). The basic principle is that the analysis and screening of features from images obtained by CT, positron emission tomography (PET)-CT, or magnetic resonance imaging can evaluate tumor heterogeneity at the cellular level (16-18), because the heterogeneity of tumor cells determines invasiveness and hence the prognosis (19,20). Therefore, descriptive and predictive models based on radiomics will help clinicians make accurate diagnoses. Relevant studies suggest that radiomics performed well in diagnosing lung cancer stage, predicting genotype and prognosis, and evaluating the efficacy of adjuvant therapy (21,22). However, there is a lack of studies on the correlation between the malignancy of lung adenocarcinoma and the imaging characteristics of nodules. This suggests that radiomics can also be used for the diagnosis of the malignancy of lung adenocarcinoma, especially small pulmonary nodules with a diameter ≤ 2 cm on imaging. Such knowledge would allow selection of the appropriate surgical approach to ensure maximum survival benefit in the case of preoperative or intraoperative rapid pathology suggestive of adenocarcinoma.

Highlight box

Key findings

- The diagnostic models based on radiomics performed well at diagnosing the degree of malignancy of lung adenocarcinoma with small nodules (≤ 2 cm in diameter) on images;
- The comprehensive diagnostic model based on the independent predictors and radiomics had better diagnostic performance.

What is known and what is new?

- As an emerging technology, radiomics is being widely used in the diagnosis of lung cancer due to its excellent diagnostic performance.
- In this study, patients with a nodule diameter ≤ 2 cm on preoperative CT images and a postoperative diagnosis of invasive adenocarcinoma were included to explore whether a diagnostic model based on radiomics could perform well in diagnosing the degree of tumor malignancy.

What is the implication, and what should change now?

- Further prospective clinical studies are needed to verify the clinical potential of the models.

In this study, patients with a nodule diameter ≤ 2 cm on preoperative CT images and a postoperative diagnosis of invasive adenocarcinoma were included to explore whether a diagnostic model established based on radiomics could perform better than a clinical model based on imaging features in diagnosing the degree of tumor malignancy. We also explored a comprehensive diagnostic model that combines traditional imaging features and radiomics to further improve the diagnostic performance and thus the potential for clinical application. We present the following article in accordance with the TRIPOD reporting checklist (available at <https://jtd.amegroups.com/article/view/10.21037/jtd-22-1520/rc>).

Methods

Selection and grouping of patients

In this retrospective study, patients who were hospitalized in the Department of Thoracic Surgery, The First Affiliated Hospital of Soochow University, between January 2020 and December 2021 and met the criteria were enrolled. Inclusion criteria were: (I) chest CT examination before surgery, and maximum diameter of the nodule on CT images (maximum transverse diameter and maximum longitudinal diameter) ≤ 2 cm; (II) surgical treatment within ≤ 7 days of CT examination; (III) complete pathological results of invasive adenocarcinoma; and (IV) complete baseline clinical data. Exclusion criteria were: (I) maximum diameter of the nodule on CT images (maximum transverse diameter or maximum longitudinal diameter) > 2 cm; (II) history of malignant tumor and distant metastasis; (III) preoperative anti-inflammatory or antitumor therapy; and (IV) poor image quality or loss of clinical data. The postoperative pathological diagnosis of the enrolled patients met the classification criteria for lung adenocarcinoma specified by the World Health Organization (WHO) (23-25).

According to the study design, patients were divided into low-risk and high-risk groups according to their postoperative routine pathological results. If the tumor contained solid or micropapillary components, some squamous cell carcinoma or mucinous adenocarcinoma components, if there was STAS, LVI, VPI, translobar growth, or lymph node metastasis, the patient was high risk. Otherwise, patients were assigned to the low-risk group (Figure 1). In addition, according to our need to establish a diagnostic mode, all enrolled patients were randomly

divided into experimental and validation groups according to the ratio of 7:3.

This study was based on retrospective studies. The study was conducted in accordance with the Declaration of Helsinki (as revised in 2013). Individual consent for this retrospective analysis was waived. The study was approved by Ethics Committees of The First Affiliated Hospital of Soochow University (No. 2022465).

Acquisition of CT images

TOSHIBA, PHILIPS, and SIEMENS CT scanners were used with the following parameters: tube voltage 120 kV, tube current 110–240 mA, real-time dynamic exposure dose adjustment, collimation 0.6×128 mm, rotation speed 0.5 s/turn, pitch factor 0.9, and scanning layer thickness of 5 mm. The patient lay supine with both arms raised and the head advanced, and was scanned at the end of inspiration. The scanning range included the thoracic entrance to 5 cm below the costophrenic angle. The lung window [window width =1,500 Hounsfield units (HU); window level =−500 HU] and mediastinal window (window width =400 HU; window level =45 HU) were reconstructed for all images, and the reconstructed slice thickness was 1 mm.

Collection of baseline clinical data and imaging features

The baseline clinical data included the patient's sex, age, smoking history, and body mass index (BMI). The imaging features included the maximum diameter and nature of the nodule, as well as special features related to the CT imaging morphology of the nodule. Mixed-density nodules and solid nodules with CTR > 0.5 are suggestive of a high degree of tumor malignancy (26-28). Therefore, we classified the nodule properties according to CTR > 0.5 to optimize the data analysis. The selected imaging features are typically used to distinguish the degree of infiltration of the lesion: lobulation, burr, vacuolar, pleural indentation, vascular anomaly, and bronchial anomaly (29). The assessment of these features was performed independently by a thoracic surgeon and a radiologist, using the following definitions.

- ❖ Lobulation: uneven or wavy surface of the nodule;
- ❖ Burr: radiating short, linear shadow with nodule edge extending toward the lung parenchyma but not reaching the pleural surface;
- ❖ Vacuolar: nodule contains circular or quasi-circular air-bearing density area;
- ❖ Pleural indentation: linear shadow originating from

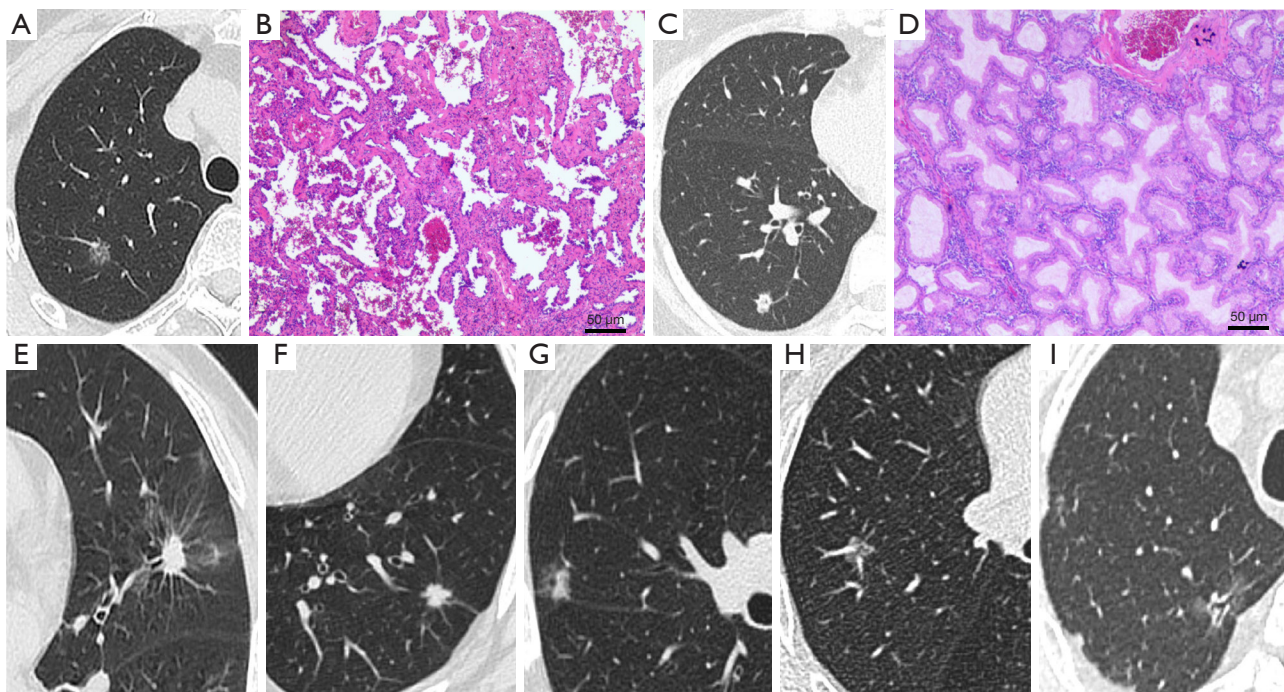


Figure 1 Examples of pathology from the high- and low-risk groups and the imaging features of the nodules. Pathological results of tissue specimens were derived based on hematoxylin-eosin staining. (A,B) Low-risk group. Pathology suggests acinar-dominant adenocarcinoma. (C,D) High-risk group. Pathology suggests mucinous adenocarcinoma. (E) Burr sign. (F) Lobulation and pleural indentation. (G) Vacuolar sign. (H) Vascular anomaly. (I) Bronchial anomaly.

the nodule and reaching the pleura or obvious pulmonary depression in the nodule adjacent to the pleura;

- ❖ Vascular anomaly: thickening, distortion of blood vessels in the nodule, or the entry of ≥ 2 connected blood vessels into the nodule;
- ❖ Bronchial anomaly: bronchus sign or intranodular bronchiectasis, distortion, and truncation.

The imaging features are shown in *Figure 1*.

Establishment of the clinical model

Firstly, the independent predictors of high-risk nodules in the baseline clinical data and imaging features were screened by univariate and multivariate analysis. Then multivariate logistic regression analysis was used to establish a nomogram as part of the clinical diagnostic model. The diagnostic performance evaluation of the clinical model was based on the ROC curve. And the clinical score (Cliscore) was calculated using the following formula: Cliscore = $-3.9758 + \text{CTR (0/1)} \times 1.9591 + \text{lobulated signs (0/1)} \times 1.9174 + \text{vascular anomaly signs (0/1)} \times 1.7119$.

Establishment of the radiomics model

Delineation of the region of interest (ROI) and extraction and screening of radiomics features

The screening of radiomics features was based on the free and open-source 3DSlicer (version 4.11.20210226) software. The thin-slice (1 mm) CT image data were imported into the 3DSlicer, and the image display was set to the lung window (window width 1,500 HU, window level -500 HU). Next, the ROI was delineated: (I) detailed delineation of some nodules with uneven or wavy edges, including short linear shadows that were involved in the burr sign and pleural depression sign; (II) delineation of the vessels and bronchi that penetrated the nodes, avoiding unrelated vascular tracheal shadows; (III) the image in each plane was delineated layer by layer. We combined these criteria to generate a three-dimensional (3D) image of the ROI.

The radiomics features of the 3D ROI images were extracted using the Radiomics software for the 3DSlicer. Radiomics features included first-order image intensity statistics, shape, gray-level co-occurrence matrix (GLCM), gray-level dependence matrix (GLDM), gray-level run-

length matrix (GLRLM), gray-level size-zone matrix (GLSZM), and neighboring gray-tone difference matrix (NGTDM). The resampling voxel size was set to 1 mm × 1 mm × 1 mm. A total of 107 radiomics features were extracted from each 3D ROI image.

The radiomics features were screened using the least absolute shrinkage and selection operator (LASSO), and the 5-fold cross-validation method was used for overfitting to improve the stability of the radiomics model.

Radiomics model construction and performance evaluation

The radiomics features selected by LASSO and the corresponding feature values were used for the construction of the radiomics model. The radiomics feature values selected were linearly combined with the corresponding LASSO coefficients to obtain the radiomics score (Radscore), which was calculated as: $\text{Radscore} = -0.943121 + \text{shape} - \text{least axis length} \times 0.0216482 + \text{shape} - \text{maximum 2D diameter column} \times 0.003900226 + \text{shape} - \text{minor axis length} \times 0.008463369 + \text{first order} - 90 \text{ percentile} \times 0.000461367 + \text{first order} - \text{mean} \times 0.00003293427 - \text{first order} - \text{skewness} \times 0.02075693 + \text{GLCM} - \text{inverse difference normalized} \times 1.150171 + \text{GLDM} - \text{large dependence high gray level emphasis} \times 0.00000583624 - \text{NGTDM} - \text{coarseness} \times 1.901466$.

Receiver operating characteristic (ROC) curves were drawn to evaluate the diagnostic performance of the radiomics model in the experimental and validation groups.

Establishment of the comprehensive model and performance evaluation

Univariate analysis was used to screen for variables with significant differences between the high- and low-risk groups in baseline clinical data and imaging characteristics. Multivariate binary logistic regression analysis was used to screen independent predictors of high-risk nodules. The nomogram of the comprehensive model comprised the independent predictors and the Radscore. The diagnostic performance evaluation of the comprehensive model was based on the ROC curve.

Decision curve analysis (DCA) was used to evaluate clinical applicability of both models. The comprehensive score (Comscore) was calculated using the following formula: $\text{Comscore} = -5.5396 + \text{CTR} (0/1) \times 0.9032 + \text{lobulated signs} (0/1) \times 1.4610 + \text{vascular anomaly signs} (0/1) \times 0.7170 + \text{Radscore} \times 6.7258$

Statistical analysis

Statistical analysis of the data was performed with SPSS (version 25) and RStudio (version 4.2.0). Baseline clinical data and imaging features were divided into continuous and categorical variables. The independent-sample *t*-test was used for continuous variables that were normally distributed, and the Mann-Whitney U test was used for those that did not conform to a normal distribution. Univariate analysis of categorical variables was performed with the χ^2 test. Multivariate analysis was performed using binary logistic regression analysis, where the categorical variable outcome was expressed as 0/1. Thus, the independent predictors of high-risk nodules in the baseline clinical data and imaging features were screened.

Using the Radscore and the independent predictors as variables, multivariate logistic regression analysis was used to establish a nomogram as part of the comprehensive diagnostic model. The diagnostic efficacy of each model was tested using the ROC curves, and the area under the curve (AUC), sensitivity, and specificity were used for evaluation. The Hosmer-Lemeshow test was used to evaluate the goodness of fit of the model and generate a calibration curve. Delong's test was used to examine the statistical differences between the ROC curves of each model in experimental and validation group. DCA was used to evaluate the clinical application potential of each model. $P < 0.05$ for both sides was considered statistically significant. The plotting of the nomogram, ROC curve, calibration curve, and DCA curve was based on the calculation code written in RStudio.

Results

Analysis of baseline clinical data and imaging features

A total of 170 patients were enrolled in the study. The experimental group consisting of 120 patients included 60 patients with high-risk lung adenocarcinoma while a total of 50 patients were included in the validation group, 20 of whom were high-risk lung adenocarcinoma patients. There was no significant difference in the incidence of high-risk lung adenocarcinoma between the two groups ($P > 0.05$).

The baseline clinical data (age, sex, smoking history, and BMI) and imaging feature data (nodule maximum diameter, nature, lobulation, burr sign, vacuolar sign, pleural indentation, vascular anomaly, bronchial anomaly) of the 170 enrolled patients are shown in *Table 1*. The results of univariate analysis in experimental group suggested that

Table 1 Baseline clinical data and imaging features of patients in the experimental group and validation group

Variables	Experimental group (n=120)			Validation group (n=50)		
	Low-risk (n=60)	High-risk (n=60)	P	Low-risk (n=30)	High-risk (n=20)	P
Age (years)	57.52±12.17	60.68±10.82	0.135	57.00±10.68	59.35±9.28	0.426
Sex, n (%)			0.141			0.077
Male	22 (36.67)	30 (50.00)		9 (30.00)	11 (55.00)	
Female	38 (63.33)	30 (50.00)		21 (70.00)	9 (45.00)	
Smoking history, n (%)			0.211			0.149
None	53 (88.33)	48 (80.00)		26 (86.67)	14 (70.00)	
Persistent or had smoked	7 (11.67)	12 (20.00)		4 (13.33)	6 (30.00)	
BMI (kg/m ²)	23.97±3.52	24.08±3.11	0.854	24.22±3.50	24.02±3.07	0.834
Nodule size (mm)	13.58±4.02	15.92±3.28	<0.001	12.87±3.45	16.05±3.11	0.002
Nodule nature, n (%)			<0.001			0.002
CTR <0.5	36 (60.00)	80 (13.33)		21 (70.00)	5 (25.00)	
CTR >0.5	24 (40.00)	52 (86.67)		9 (30.00)	15 (75.00)	
Lobulation, n (%)			<0.001			0.012
None	28 (46.67)	4 (6.67)		15 (50.00)	3 (15.00)	
Yes	32 (53.33)	56 (93.33)		15 (50.00)	17 (85.00)	
Burr sign, n (%)			<0.001			0.009
None	41 (68.33)	15 (25.00)		23 (76.67)	8 (40.00)	
Yes	19 (31.67)	45 (75.00)		7 (23.33)	12 (60.00)	
Vacuolar sign, n (%)			0.673			0.149
None	46 (76.67)	44 (73.33)		26 (86.67)	14 (70.00)	
Yes	14 (23.33)	16 (26.67)		4 (13.33)	6 (30.00)	
Pleural indentation, n (%)			0.007			0.133
None	28 (46.67)	14 (23.33)		17 (56.67)	7 (35.00)	
Yes	32 (53.33)	46 (76.67)		13 (43.33)	13 (65.00)	
Bronchial anomaly, n (%)			0.014			0.012
None	44 (73.33)	31 (51.67)		26 (86.67)	11 (55.00)	
Yes	16 (26.67)	29 (48.33)		4 (13.33)	9 (45.00)	
Vascular anomaly, n (%)			<0.001			0.015
None	29 (48.33)	10 (16.67)		18 (60.00)	5 (25.00)	
Yes	31 (51.67)	50 (83.33)		12 (40.00)	15 (75.00)	

Continuous variables are expressed using the mean ± standard deviation. P<0.05 was statistically significant. BMI, body mass index; CTR, consolidation-to-tumor ratio.

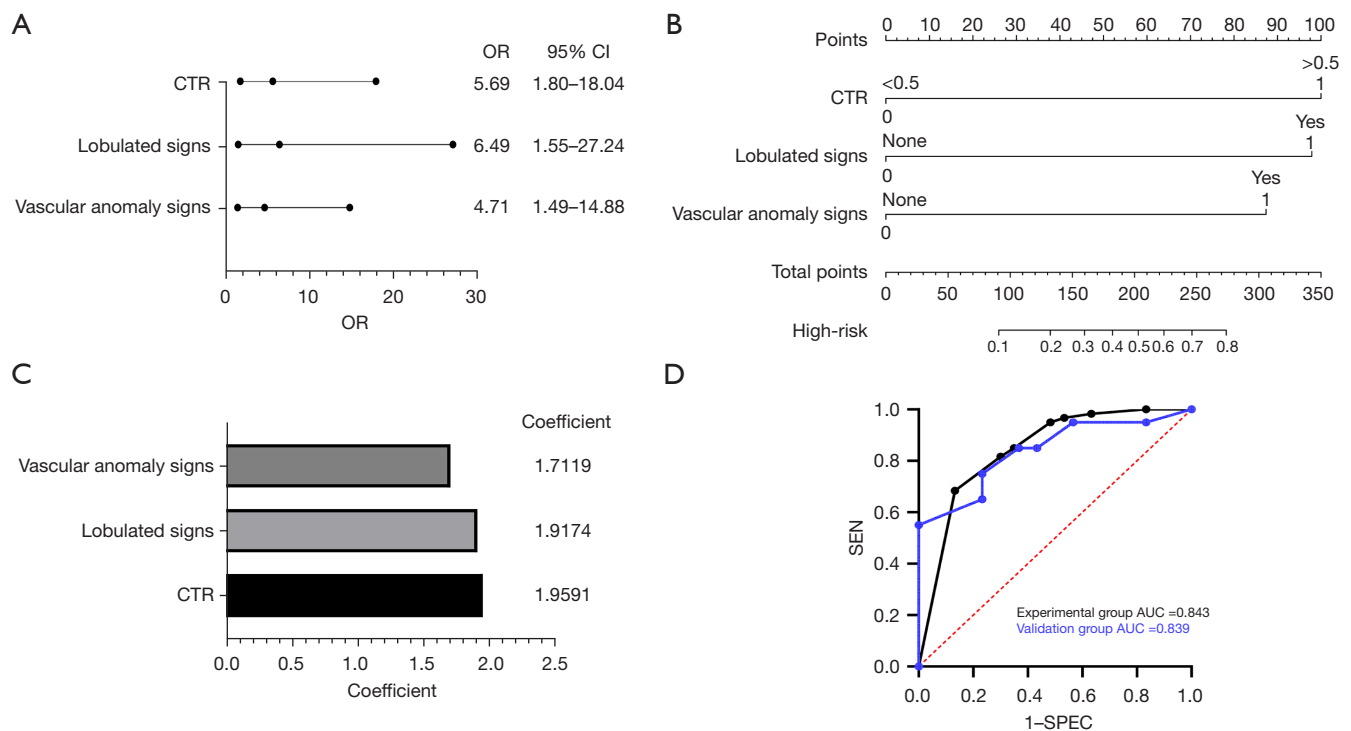


Figure 2 Establishment of clinical models and evaluation of diagnostic performance. (A) Results of multivariate logistic regression analysis of baseline clinical data and imaging feature data. (B) Nomogram of the clinical diagnostic model. (C) Clinical diagnostic model components and corresponding feature values. (D) ROC curves of the clinical diagnostic model for the experimental and validation groups. CTR, consolidation-to-tumor ratio; OR, odds ratio; CI, confidence interval; SEN, sensitivity; SPEC, specificity; AUC, area under the curve; ROC, receiver operating characteristic.

nodule size ($P < 0.001$), nodule nature ($P < 0.001$), lobulation ($P < 0.001$), burr ($P < 0.001$), pleural indentation ($P = 0.007$), bronchial anomaly ($P < 0.014$), and vascular anomaly ($P < 0.001$) were significantly different between the high- and low-risk groups.

Establishment of the clinical model and evaluation of diagnostic performance

The significant variables in the univariate analysis were included in multivariate binary logistic regression analysis. The results showed that patients were more likely to have high-risk nodules when they had a nodal CTR > 0.5 [odds ratio (OR): 5.69, 95% confidence interval (CI): 1.80–18.04], lobulated signs (OR: 6.49, 95% CI: 1.55–27.24), and vascular anomaly signs (OR: 4.71, 95% CI: 1.49–14.88) (Figure 2A). The clinical diagnostic model was constructed by combining independent predictors (CTR > 0.5 , lobulation signs, and vascular anomaly signs) and a nomogram was plotted based on multivariate logistic regression (Figure 2B).

The components of the clinical diagnostic model and the corresponding feature values are shown in Figure 2C.

The ROC curves of the clinical diagnostic model for the experimental and validation groups are shown in Figure 2D. The AUC of the clinical diagnostic model for the experimental group was 0.843 (95% CI: 0.771–0.913), with sensitivity of 68.3% and specificity of 86.7%. The AUC for the validation group was 0.839 (95% CI: 0.720–0.958), with sensitivity of 70.0% and specificity of 76.7%.

Establishment of the radiomics model and evaluation of diagnostic performance

In the experimental group, nine optimal imaging radiomics features were screened from the 107 extracted features using LASSO. The corresponding LASSO coefficients are shown in Figure 3.

The distribution of the Radscore among all patients in the experimental group is shown in Figure 4A. The Radscore of the high-risk group was significantly higher

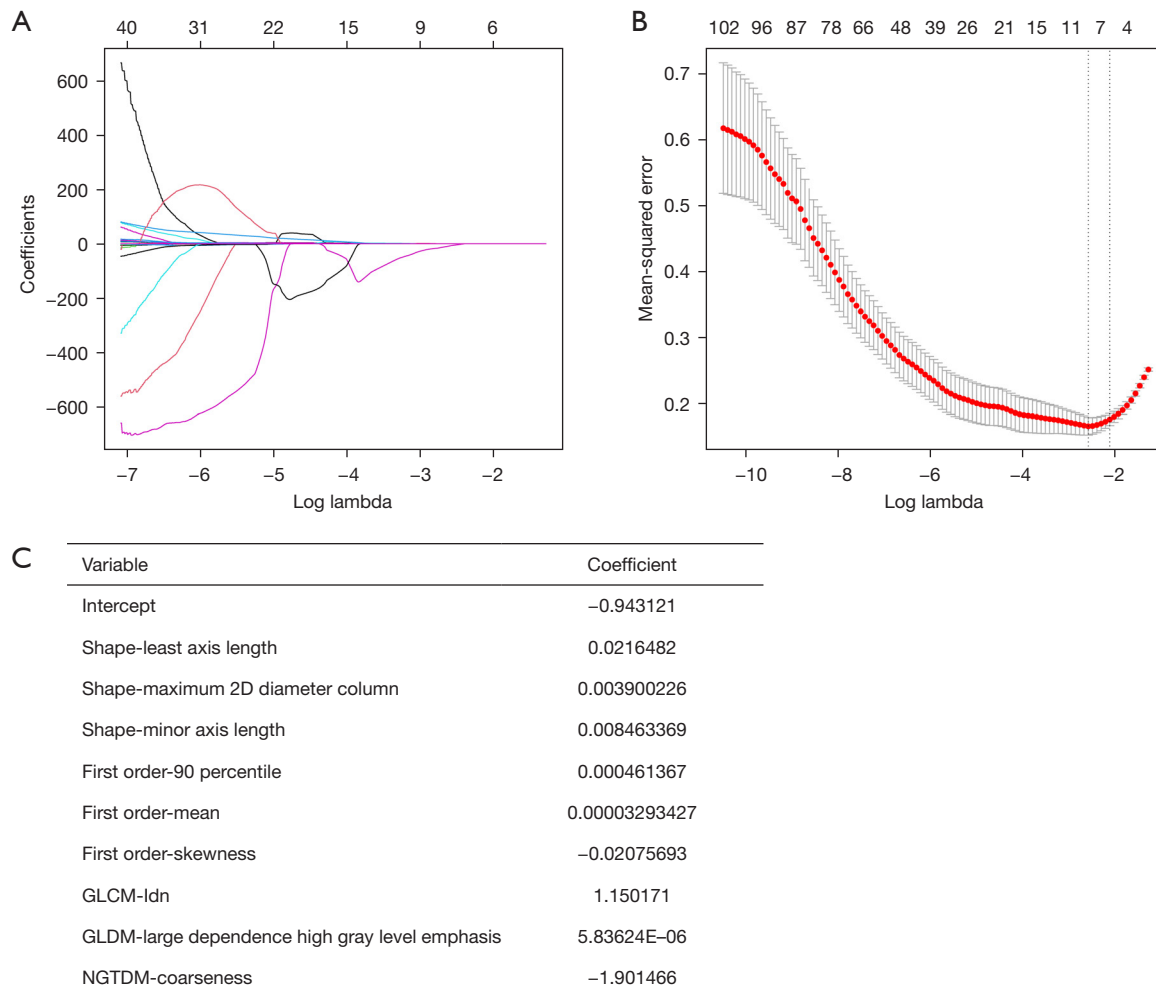


Figure 3 Screening of radiomics features in the experimental group by LASSO regression. (A) LASSO coefficient profile of radiomics features. (B) Optimal feature selection based on mean squared error. (C) Optimal radiomics features and corresponding LASSO coefficients. 2D, two-dimensional; GLCM, gray-level co-occurrence matrix; Idn, inverse difference normalized; NGTDM, neighboring gray-tone difference matrix; LASSO, least absolute shrinkage and selection operator.

than that of the low-risk group ($P < 0.001$). The ROC curve of the radiomics model of the experimental group is shown in *Figure 4B*. It had an AUC of 0.898 (95% CI: 0.843–0.953), with diagnostic sensitivity of 76.7% and specificity of 91.7%. The distribution of the Radscore among all patients in the validation group is shown in *Figure 4C*, and the ROC curve of the radiomics model in the is shown in *Figure 4D*. It had an AUC of 0.926 (95% CI: 0.857–0.995), with diagnostic sensitivity of 80.0% and specificity of 90.0%. These results showed good diagnostic performance of the constructed radiomics model for differentiating the risk level of nodules.

Establishment of the comprehensive diagnostic model and evaluation of diagnostic performance

The comprehensive diagnostic model was constructed by combining the independent predictors (CTR > 0.5 , lobulation, and vascular anomaly) and the Radscore, and a nomogram was plotted based on multivariate logistic regression (*Figure 5A*). The components of the comprehensive diagnostic model and the corresponding feature values are shown in *Figure 5B*.

The ROC curves of the comprehensive diagnostic model for the experimental and validation groups are shown in

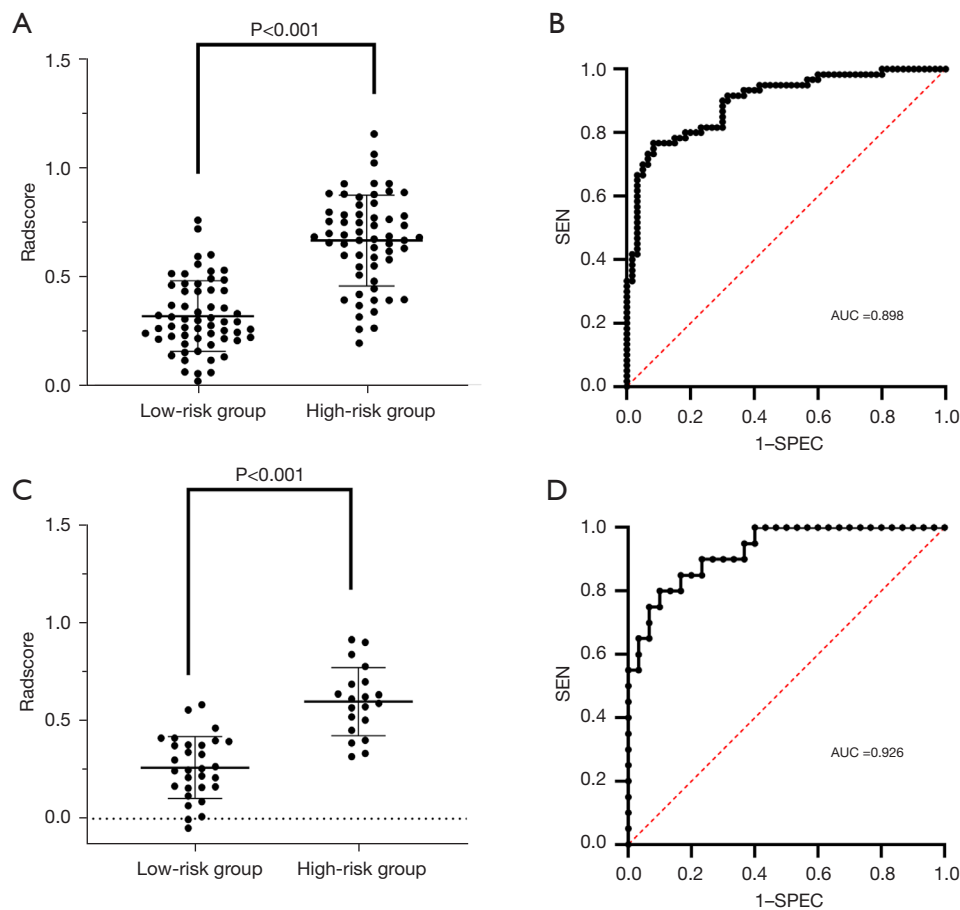


Figure 4 Distribution of the Radscore in the experimental group (A) and the validation group (C). ROC curve of the radiomics model in the experimental group (B) and the validation group (D). SEN, sensitivity; SPEC, specificity; AUC, area under the curve; ROC, receiver operating characteristic.

Figure 5C. The AUC of the comprehensive diagnostic model for the experimental group was 0.919 (95% CI: 0.873–0.966), with sensitivity of 78.3% and specificity of 90.0%. The AUC for the validation group was 0.922 (95% CI: 0.851–0.992), with sensitivity of 85.0% and specificity of 80.0%. These results showed that the comprehensive diagnostic model had good diagnostic performance. The calibration curves of the comprehensive diagnostic model showed good predictive consistency in both the experimental and validation groups (*Figure 5D, 5E*).

Comparison of the diagnostic performance of each model

The diagnostic performance of each model is shown in *Table 2*. The diagnostic performance of radiomics model and comprehensive model is better than clinical diagnostic

model (DeLong's test, $P < 0.05$). The ROC curves of each diagnostic model for the experimental and validation groups are shown in *Figure 6A, 6B*. The DCA curves of radiomics model and comprehensive model suggested they had good net survival benefit and some potential for clinical application (*Figure 6C, 6D*).

Discussion

Compared with clinical model (AUC 0.839, 95% CI: 0.720–0.958), radiomics model (AUC 0.926, 95% CI: 0.857–0.995) performed well at diagnosing the degree of malignancy of lung adenocarcinoma with small nodules (≤ 2 cm in diameter) on images. The comprehensive diagnostic model based on the independent predictors and radiomics model had good diagnostic performance (AUC 0.922, 95%

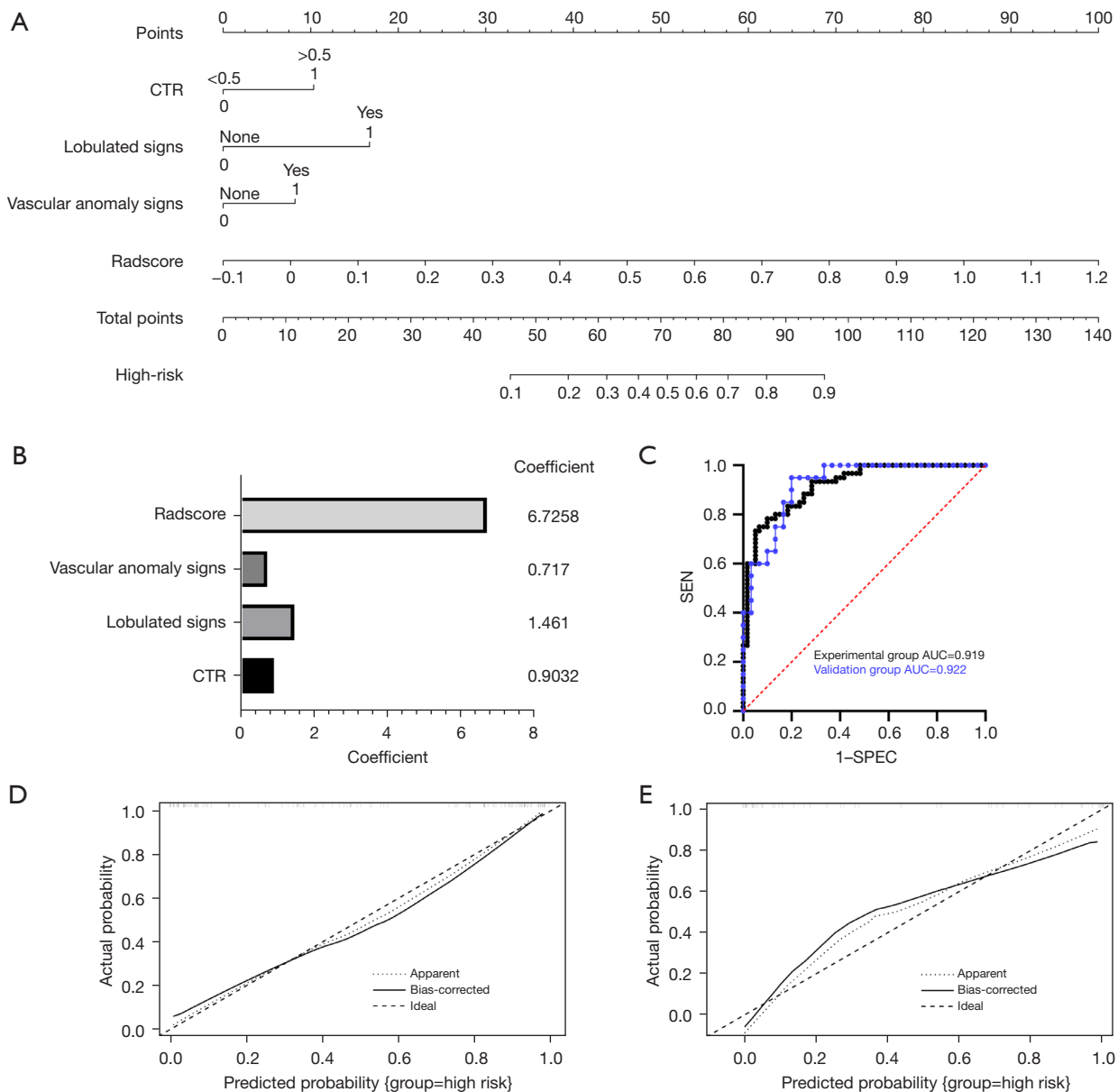


Figure 5 Establishment of comprehensive models and evaluation of diagnostic performance. (A) Nomogram of the comprehensive diagnostic model. (B) Comprehensive diagnostic model components and corresponding feature values. (C) ROC curves of the comprehensive diagnostic model for the experimental and validation groups. Calibration curves for the experimental group (D) and the validation group (E). CTR, consolidation-to-tumor ratio; SEN, sensitivity; SPEC, specificity; AUC, area under the curve; ROC, receiver operating characteristic.

CI: 0.851–0.992) and thus has some clinical application potential.

Smoking, male sex, and advanced age (≥ 70 years) are high-risk factors for lung cancer (30,31), but not in this study for high risk of invasive lung adenocarcinoma. One reason for this discrepancy is that as CT imaging technology advances, small pulmonary nodules are being

found more often in younger populations. In this study, both the high-risk group and low-risk group had a mean age < 65 years. Invasive lung adenocarcinoma is more common in women, and its incidence is increasing every year (32). In this study, women accounted for 57.6% of all patients enrolled. Smoking is considered to be closely related to the occurrence of lung squamous cell carcinoma, and the

majority of smokers in the Chinese population are male (31). In this study, the proportion of smokers in the male population was 37.5%.

We found that the burr, vacuole, pleural indentation, and bronchial anomaly signs were not risk factors for high-risk

Table 2 The diagnostic performance of clinical model, Radscore model and comprehensive model

Model	AUC (95% CI)	SEN	SPEC
Experimental group			
Clinical model	0.843 (0.771, 0.913)	0.683	0.867
Radscore model	0.898 (0.843, 0.953)	0.767	0.917
Comprehensive model	0.919 (0.873, 0.966)	0.783	0.900
Validation group			
Clinical model	0.839 (0.720, 0.958)	0.700	0.767
Radscore model	0.926 (0.857, 0.995)	0.800	0.900
Comprehensive model	0.922 (0.851, 0.992)	0.850	0.800

AUC, area under the curve; CI, confidence interval; SEN, sensitivity; SPEC, specificity.

nodules, but CTR >0.5, lobulation and vascular anomaly suggested high-risk nodules. Thus, we constructed a clinical model based on CTR, lobulated signs and vascular anomaly signs. The AUCs of the clinical diagnostic model in the experimental and validation groups were 0.843 and 0.839, respectively. Therefore, predicting the malignancy of lung adenocarcinoma based on clinical models alone remains a great challenge. This study focused on investigating the correlation between the malignancy of lung adenocarcinoma and the imaging features, which sets it apart from existing studies. Most studies on the imaging characteristics of pulmonary nodules have investigated the differences in imaging characteristics between preinvasive and invasive lesions, and there is a lack of studies on the correlation between the malignancy of early lung cancer and the imaging characteristics of nodules. Gao *et al.* (33) and Song *et al.* (34) found that pulmonary nodules with abnormal vascular penetration and small vacuoles were more likely to be invasive lung cancer. Xing *et al.* (35) found that nodules with the lobulated and burr signs are indicators of invasive lung cancer. Yan *et al.* (36) found that nodules with pleural indentation on CT images were more likely to be invasive

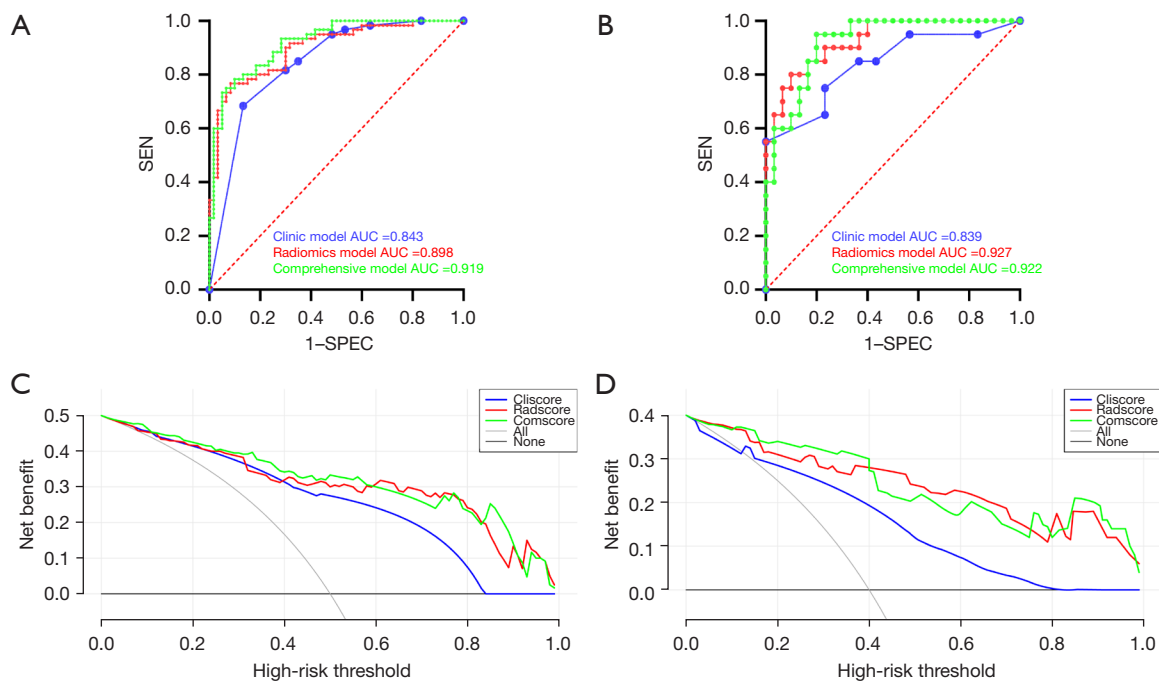


Figure 6 Evaluation of the diagnostic performance and clinical application potential of each model. ROC curves of each diagnostic model for the experimental group (A) and validation group (B). DCA curves of each diagnostic model for the experimental group (C) and validation group (D). SEN, sensitivity; SPEC, specificity; AUC, area under the curve; ROC, receiver operating characteristic; DCA, decision curve analysis.

lung cancer. Mixed-density ground-glass nodules with CTR >0.5 on CT images are more likely to be invasive lung cancer, and invasive lung cancers with solid nodules on CT images have a higher degree of malignancy (26).

In recent years, the application of radiomics to the diagnosis of lung cancer has attracted more attention (21,37). Choi *et al.* (16) showed that radiomics can reflect the pathological heterogeneity of lung cancer cells and thus predict the degree of tumor malignancy. Soon after, Xue *et al.* (38) and Sun *et al.* (39) showed that radiomics has good diagnostic performance in distinguishing the degree of infiltration of lung cancer with ground-glass nodules on imaging. Radiomics has performed well at distinguishing between benign and malignant subtypes of solid nodules and pathological subtypes (40).

Compared with previous studies, our research was innovative, firstly in the selection of study subjects. We were not limited to distinguishing between benign and malignant pulmonary nodules or whether there was infiltration in early lesions. Secondly, we grouped patients as high- or low-risk for lung adenocarcinoma with small nodules (≤ 2 cm in diameter) on CT images. Patients with STAS, LVI, VPI, translobar growth, or lymph node metastasis were classified as the high-risk group according to published findings (7-9,11,13,14). Thirdly, the extraction of radiomics features was not limited to CT images at a certain level; in this study, the nodule images of each plane were delineated layer by layer to generate 3D ROI images for the extraction of radiomics features. We constructed a comprehensive diagnostic model by combining traditional imaging features with radiomics features to further improve the clinical application potential of the model. Compared with clinical model, our radiomics model and comprehensive diagnostic model both performed well for the diagnosis of malignant degree of lung adenocarcinoma. and have the potential for clinical application.

This study has some limitations. (I) It was a retrospective study, so it inevitably had selection bias. (II) It was a single-center study, with a small overall sample size. Large, multicenter validation studies are needed. (III) The ROIs were manually delineated, without a standardized image acquisition process. The CT images were obtained from multiple devices, which may cause some bias. (IV) The classification criteria in this study relied on postoperative pathology, and the sample distribution was biased.

Conclusions

Compared with clinical models, the radiomics-based model presented here performed well at diagnosing malignant degree of lung adenocarcinoma. The comprehensive diagnostic model made up of independent predictors and radiomics features has good diagnostic performance and thus has some potential for clinical application. We believe that for low-risk patients (as suggested by the diagnostic model constructed in this study) segmentectomy can be chosen as the standard surgical procedure, whereas lobectomy is more likely to ensure a survival benefit in patients at high risk. Further prospective clinical studies can verify the clinical potential of the models.

Acknowledgments

Funding: This study was supported by the Suzhou Science and Technology Project (No. SS2019014).

Footnote

Reporting Checklist: The authors have completed the TRIPOD reporting checklist. Available at <https://jtd.amegroups.com/article/view/10.21037/jtd-22-1520/rc>

Data Sharing Statement: Available at <https://jtd.amegroups.com/article/view/10.21037/jtd-22-1520/dss>

Conflicts of Interest: All authors have completed the ICMJE uniform disclosure form (available at <https://jtd.amegroups.com/article/view/10.21037/jtd-22-1520/coif>). The authors have no conflicts of interest to declare.

Ethical Statement: The authors are accountable for all aspects of the work in ensuring that questions related to the accuracy or integrity of any part of the work are appropriately investigated and resolved. The study was conducted in accordance with the Declaration of Helsinki (as revised in 2013). Individual consent for this retrospective analysis was waived. The study was approved by Ethics Committees of The First Affiliated Hospital of Soochow University (No. 2022465).

Open Access Statement: This is an Open Access article

distributed in accordance with the Creative Commons Attribution-NonCommercial-NoDerivs 4.0 International License (CC BY-NC-ND 4.0), which permits the non-commercial replication and distribution of the article with the strict proviso that no changes or edits are made and the original work is properly cited (including links to both the formal publication through the relevant DOI and the license). See: <https://creativecommons.org/licenses/by-nc-nd/4.0/>.

References

1. CAHAN WG. Radical lobectomy. *J Thorac Cardiovasc Surg* 1960;39:555-72.
2. Ginsberg RJ, Rubinstein LV. Randomized trial of lobectomy versus limited resection for T1 N0 non-small cell lung cancer. Lung Cancer Study Group. *Ann Thorac Surg* 1995;60:615-22; discussion 622-3.
3. Shen H. Low-dose CT for lung cancer screening: opportunities and challenges. *Front Med* 2018;12:116-21.
4. Suzuki K. Whack-a-mole strategy for multifocal ground glass opacities of the lung. *J Thorac Dis* 2017;9:S201-7.
5. Suzuki K, Watanabe SI, Wakabayashi M, et al. A single-arm study of sublobar resection for ground-glass opacity dominant peripheral lung cancer. *J Thorac Cardiovasc Surg* 2022;163:289-301.e2.
6. Saji H, Okada M, Tsuboi M, et al. Segmentectomy versus lobectomy in small-sized peripheral non-small-cell lung cancer (JCOG0802/WJOG4607L): a multicentre, open-label, phase 3, randomised, controlled, non-inferiority trial. *Lancet* 2022;399:1607-17.
7. Choi SH, Jeong JY, Lee SY, et al. Clinical implication of minimal presence of solid or micropapillary subtype in early-stage lung adenocarcinoma. *Thorac Cancer* 2021;12:235-44.
8. Warth A, Muley T, Meister M, et al. The novel histologic International Association for the Study of Lung Cancer/American Thoracic Society/European Respiratory Society classification system of lung adenocarcinoma is a stage-independent predictor of survival. *J Clin Oncol* 2012;30:1438-46.
9. Chae M, Jeon JH, Chung JH, et al. Prognostic significance of tumor spread through air spaces in patients with stage IA part-solid lung adenocarcinoma after sublobar resection. *Lung Cancer* 2021;152:21-6.
10. Eguchi T, Kameda K, Lu S, et al. Lobectomy Is Associated with Better Outcomes than Sublobar Resection in Spread through Air Spaces (STAS)-Positive T1 Lung Adenocarcinoma: A Propensity Score-Matched Analysis. *J Thorac Oncol* 2019;14:87-98.
11. Lee MA, Kang J, Lee HY, et al. Spread through air spaces (STAS) in invasive mucinous adenocarcinoma of the lung: Incidence, prognostic impact, and prediction based on clinicoradiologic factors. *Thorac Cancer* 2020;11:3145-54.
12. Wang S, Zhang B, Qian J, et al. Proposal on incorporating lymphovascular invasion as a T-descriptor for stage I lung cancer. *Lung Cancer* 2018;125:245-52.
13. Higgins KA, Chino JP, Ready N, et al. Lymphovascular invasion in non-small-cell lung cancer: implications for staging and adjuvant therapy. *J Thorac Oncol* 2012;7:1141-7.
14. Wo Y, Zhao Y, Qiu T, et al. Impact of visceral pleural invasion on the association of extent of lymphadenectomy and survival in stage I non-small cell lung cancer. *Cancer Med* 2019;8:669-78.
15. Kumar V, Gu Y, Basu S, et al. Radiomics: the process and the challenges. *Magn Reson Imaging* 2012;30:1234-48.
16. Choi ER, Lee HY, Jeong JY, et al. Quantitative image variables reflect the intratumoral pathologic heterogeneity of lung adenocarcinoma. *Oncotarget* 2016;7:67302-13.
17. Sala E, Mema E, Himoto Y, et al. Unravelling tumour heterogeneity using next-generation imaging: radiomics, radiogenomics, and habitat imaging. *Clin Radiol* 2017;72:3-10.
18. Mayerhoefer ME, Materka A, Langs G, et al. Introduction to Radiomics. *J Nucl Med* 2020;61:488-95.
19. Burrell RA, McGranahan N, Bartek J, et al. The causes and consequences of genetic heterogeneity in cancer evolution. *Nature* 2013;501:338-45.
20. Zuo S, Wei M, Wang S, et al. Pan-Cancer Analysis of Immune Cell Infiltration Identifies a Prognostic Immune-Cell Characteristic Score (ICCS) in Lung Adenocarcinoma. *Front Immunol* 2020;11:1218.
21. Wilson R, Devaraj A. Radiomics of pulmonary nodules and lung cancer. *Transl Lung Cancer Res* 2017;6:86-91.
22. Thawani R, McLane M, Beig N, et al. Radiomics and radiogenomics in lung cancer: A review for the clinician. *Lung Cancer* 2018;115:34-41.
23. Kuhn E, Morbini P, Cancellieri A, et al. Adenocarcinoma classification: patterns and prognosis. *Pathologica* 2018;110:5-11.
24. Travis WD, Brambilla E, Noguchi M, et al. International association for the study of lung cancer/american thoracic society/european respiratory society international multidisciplinary classification of lung adenocarcinoma. *J Thorac Oncol* 2011;6:244-85.
25. Nicholson AG, Tsao MS, Beasley MB, et al. The 2021

- WHO Classification of Lung Tumors: Impact of Advances Since 2015. *J Thorac Oncol* 2022;17:362-87.
26. Sun K, You A, Wang B, et al. Clinical T1aN0M0 lung cancer: differences in clinicopathological patterns and oncological outcomes based on the findings on high-resolution computed tomography. *Eur Radiol* 2021;31:7353-62.
 27. Suzuki S, Sakurai H, Yotsukura M, et al. Clinical Features of Ground Glass Opacity-Dominant Lung Cancer Exceeding 3.0 cm in the Whole Tumor Size. *Ann Thorac Surg* 2018;105:1499-506.
 28. Katsumata S, Aokage K, Ishii G, et al. Pathological features and prognostic implications of ground-glass opacity components on computed tomography for clinical stage I lung adenocarcinoma. *Surg Today* 2021;51:1188-202.
 29. Li Q, Fan L, Cao ET, et al. Quantitative CT analysis of pulmonary pure ground-glass nodule predicts histological invasiveness. *Eur J Radiol* 2017;89:67-71.
 30. Bade BC, Dela Cruz CS. Lung Cancer 2020: Epidemiology, Etiology, and Prevention. *Clin Chest Med* 2020;41:1-24.
 31. Wu F, Wang L, Zhou C. Lung cancer in China: current and prospect. *Curr Opin Oncol* 2021;33:40-6.
 32. Bray F, Ferlay J, Soerjomataram I, et al. Global cancer statistics 2018: GLOBOCAN estimates of incidence and mortality worldwide for 36 cancers in 185 countries. *CA Cancer J Clin* 2018;68:394-424.
 33. Gao F, Sun Y, Zhang G, et al. CT characterization of different pathological types of subcentimeter pulmonary ground-glass nodular lesions. *Br J Radiol* 2019;92:20180204.
 34. Song L, Xing T, Zhu Z, et al. Hybrid Clinical-Radiomics Model for Precisely Predicting the Invasiveness of Lung Adenocarcinoma Manifesting as Pure Ground-Glass Nodule. *Acad Radiol* 2021;28:e267-77.
 35. Xing Y, Li Z, Jiang S, et al. Analysis of pre-invasive lung adenocarcinoma lesions on thin-section computerized tomography. *Clin Respir J* 2015;9:289-96.
 36. Yan H, Hua Y, Zhang T, et al. Differential Diagnosis of Preinvasive Lesions in Small Pulmonary Nodules by Dual Source Computed Tomography Imaging. *Comput Math Methods Med* 2022;2022:6255024.
 37. Avanzo M, Stancanello J, Pirrone G, et al. Radiomics and deep learning in lung cancer. *Strahlenther Onkol* 2020;196:879-87.
 38. Xue X, Yang Y, Huang Q, et al. Use of a Radiomics Model to Predict Tumor Invasiveness of Pulmonary Adenocarcinomas Appearing as Pulmonary Ground-Glass Nodules. *Biomed Res Int* 2018;2018:6803971.
 39. Sun Y, Li C, Jin L, et al. Radiomics for lung adenocarcinoma manifesting as pure ground-glass nodules: invasive prediction. *Eur Radiol* 2020;30:3650-9.
 40. Digumarthy SR, Padole AM, Gullo RL, et al. Can CT radiomic analysis in NSCLC predict histology and EGFR mutation status? *Medicine (Baltimore)* 2019;98:e13963.
- (English Language Editor: K. Brown)

Cite this article as: Shi L, Yang M, Yao J, Ni H, Shao H, Feng W, He Z, Ni B. Application of computed tomography-based radiomics combined with clinical factors in the diagnosis of malignant degree of lung adenocarcinoma. *J Thorac Dis* 2022;14(11):4435-4448. doi: 10.21037/jtd-22-1520